separations

MDPI

Article

Comparative Investigation of Natural Mineral-Supported Li/Al-LDHs Adsorbents for Lithium Recovery from High Mg/Li Ratio Brines

Ping Liu [1,*], Chuntao Zhang [1], Jun Guo [1], Fangyuan Yu [2] and Xu Ma [3]

[1] Key Laboratory of Hubei Province for Coal Conversion and New Carbon Materials, School of Chemistry and Chemical Engineering, Wuhan University of Science and Technology, Wuhan 430081, China; zhangchuntao@wust.edu.cn (C.Z.); 202122703001@wust.edu.cn (J.G.)
[2] Jiangsu Suqing Water Treatment Engineering Group Co., Ltd., Jiangyin 214400, China; 13801525514@163.com
[3] China Chemical Safety Association, Beijing 100026, China; maxu@ccsa.net.cn
* Correspondence: liuping@ccsa.net.cn

Abstract

Lithium recovery from salt lake brines with high Mg/Li ratios remains highly challenging due to the comparable physicochemical properties of Mg^{2+} and Li^{+}, while lithium–aluminum-layered double hydroxides (Li/Al-LDHs) have emerged as promising lithium-selective adsorbents. However, their practical application is hindered by particle aggregation, limited structural stability, and insufficient processability under continuous-flow conditions. Herein, a mineral-directed synthesis strategy was developed to construct natural mineral-supported Li/Al-LDHs composite adsorbents using three abundant clay minerals, chlorite, montmorillonite, and illite, as structural substrates. The mineral crystal structures were demonstrated to regulate the nucleation, growth behavior, and dispersion of Li/Al-LDH nanosheets, resulting in distinct hierarchical architectures and lithium adsorption performances. Comprehensive structural characterization revealed the successful integration of Li/Al-LDH phases with different mineral matrices while preserving the intrinsic layered structures of both components. The results demonstrated that different mineral substrates significantly influenced the crystal growth, dispersion, and interfacial structure of Li/Al-LDHs. Among the prepared composites, montmorillonite @Li/Al-LDHs exhibited the optimal lithium adsorption performance, achieving a lithium adsorption capacity of 6.0 $mg \cdot g^{-1}$ and a remarkable Li^{+}/Mg^{2+} separation factor of 73.5 in a brine with a high Mg/Li ratio of 61.25. Furthermore, the optimized adsorbent maintained 81.7% of its initial adsorption capacity after 100 adsorption–desorption cycles and demonstrated stable lithium recovery performance under continuous-flow conditions. This work establishes the relationship between natural mineral crystal structures and Li/Al-LDH adsorption behaviors, providing new insights into the rational design of economical, scalable, and environmentally friendly lithium adsorbents for sustainable recovery of lithium resources from Mg-rich brines.

Keywords: lithium recovery; Li/Al-layered double hydroxides (Li/Al-LDHs); natural mineral-supported adsorbents; salt lake brines

Check for updates

Academic Editor: Chunlin He

Received: 18 August 2026
Revised: 10 September 2026
Accepted: 11 September 2026
Published: 13 September 2026

Copyright: © 2026 by the authors. Licensee MDPI, Basel, Switzerland. This article is an open access article distributed under the terms and conditions of the Creative Commons Attribution (CC BY) license.

1. Introduction

Lithium is the cornerstone of modern energy storage, driving the exponential growth of electric vehicles and renewable energy systems [1,2]. As global demand surges, continental salt lake brines have emerged as critical liquid resources due to their vast reserves and

cost-effectiveness [3]. However, it is still thermodynamically and kinetically demanding to extract lithium from salt lake brines, especially with an extraordinarily high Mg/Li ratio. Traditional extraction paradigms, including precipitation, solvent extraction, and membrane separation, are frequently hindered by high energy penalties, complex processing, and inadequate selectivity, necessitating the development of robust and highly selective extraction technologies [4–6].

Adsorption offers an energy-efficient and sustainable alternative for complex brine processing [7]. It operates under ambient conditions, thus avoiding the high energy input required for thermal precipitation or high-pressure membrane systems. It eliminates the use of organic solvents and large volumes of chemical reagents, reducing secondary waste streams. Furthermore, the adsorbent can be regenerated and reused over multiple cycles, minimizing material consumption per unit of lithium recovered. Among the advanced adsorbents, lithium–aluminum-layered double hydroxides (Li/Al-LDHs) exhibit exceptional ion-sieve performance [8,9]. Their unique mechanism relies on the reversible intercalation of Li^+ into specific structural vacancies within the $[Al_2(OH)_6]$ framework, which perfectly matches the unhydrated size of Li^+ while strictly excluding larger solvated competing ions like Mg^{2+} [10]. Nevertheless, the practical deployment of pristine Li/Al-LDHs is severely bottlenecked by their intrinsic structural limitations [11]. Rapid, uncontrolled crystallite growth leads to severe agglomeration that buries active sites, while their poor mechanical stability during continuous adsorption–desorption cycles largely precludes industrial column applications [12].

Compound LDHs with natural clay minerals present a compelling strategy to overcome these macroscopic deficits [13,14]. Clays are abundant, mechanically robust, and possess rich surface hydroxyl groups, making them ideal structural supports [15]. More critically, their diverse crystallographic architectures and distinct surface charge densities offer unique microenvironments that can direct the heterogeneous nucleation and hierarchical assembly of Li/Al-LDH domains [16–19]. However, previous studies mainly regarded mineral materials as carriers and lacked in-depth research on how minerals regulate the structural evolution of composite adsorbents and lithium adsorption performance [20,21]. This limitation hindered the rational design of mineral carrier-type lithium adsorbents, thereby preventing the improvement of their adsorption capacity, selectivity, and operational stability.

Herein, we proposed a systematic mineral-directed growth strategy to synthesize a family of natural mineral-supported Li/Al-LDH composites engineered for continuous lithium recovery from high Mg/Li brines. Three representative clay minerals, including montmorillonite, illite, and chlorite, were selected as structural substrates to investigate the effect of mineral characteristics on Li/Al-LDH nucleation, morphology, and adsorption behavior. The resulting composites are comprehensively characterized by XRD, SEM, BET, and XPS, and their lithium recovery performance is evaluated through batch adsorption, ion selectivity, and continuous-flow column tests. This comparative investigation not only provides foundational insights into mineral-regulated nucleation mechanisms but also delivers a highly scalable, sustainable material platform for commercial lithium extraction from complex saline resources.

2. Experimental Section

2.1. Chemical Reagents

Lithium chloride (LiCl, AR, Nanjing Chemical Reagent Co., Ltd., Nanjing, China), aluminum chloride hexahydrate ($AlCl_3 \cdot 6H_2O$, AR, Guangzhou Chemical Reagent Factory, Guangzhou, China), sodium carbonate (Na_2CO_3, Guangzhou Chemical Reagent Factory), lithium carbonate (Li_2CO_3, AR, Shanghai Kolaman Reagent Co., Ltd., Shanghai, China),

sodium chloride (NaCl, Tianjin Hengxing Chemical Reagent Manufacturing Co., Ltd., Tianjin, China), aluminum oxide (Al_2O_3, AR, Shanghai Kolaman Reagent Co., Ltd., Shanghai, China) and sodium hydroxide (NaOH, AR, Titan Technology, Nanjing, China) were of analytical grade. Natural minerals including montmorillonite, illite, and chlorite were purified and sieved (200 mesh) prior to use. All adsorption experiments were carried out using brine sourced from the Qinghai Yiliping Salt Lake (Qinghai, China) with the following composition: Li^+ (0.240 g·L^{-1}), Na^+ (0.089 g·L^{-1}), K^+ (0.005 g·L^{-1}), Ca^{2+} (0.015 g·L^{-1}), and Mg^{2+} (14.7 g·L^{-1}).

2.2. Synthesis of Li/Al-LDH–Natural Mineral Powder and Granulation

LiCl (26 g), $AlCl_3 \cdot 6H_2O$ (250 g), alumina (20 g) (Li/Al molar ratio = 1:2), and 552 mL deionized water were mixed and stirred vigorously to form a solution. Sodium carbonate (106 g), sodium chloride (30 g), lithium carbonate (95 g) (Na/Li molar ratio = 1:1), and 462 mL deionized water were mixed and stirred to form the other solution. The two solutions were mixed, and 80 g of natural mineral (montmorillonite, illite, and chlorite) powder and 200 g of hydrochloric acid (30 wt%) were added and then stirred at 100 °C and 800 rpm for 8 h. The gels were aged without heating for 24 h, washed and centrifuged with deionized water at 60 °C three times. Then the gels were granulated by incorporating them into the crosslinked copolymer of styrene and butyl acrylate (mass ratio = 2:1), and ethyl acetate was added as a pore-forming agent and stirred at 60 °C for 24 h. Stop stirring when the estimated Li/Al-LDH–natural mineral size in granulation was approximately 0.4–1.0 mm. The granulated Li/Al-LDH–natural mineral composites were filtered and dried before the subsequent adsorption experiments. Prior to the adsorption experiments, the synthesized Li/Al-LDH–natural mineral composites were thoroughly washed with deionized water.

2.3. Characterization

Surface morphologies of the samples were obtained by SEM (Phenom XL, Phenom Scientific Instruments (Shanghai) Co., Ltd., Shanghai, China). Nitrogen physisorption at 77.35 K on a Novaseries BET analyzer (Quantachrome Instruments, Boynton Beach, FL, USA) was employed to assess specific surface area and porosity. Quantification of Li^+ was performed using ICP-OES (HKYT-799, Beijing Huake Yitong Analytical Instruments Co., Ltd., Beijing, China). FTIR spectra were acquired on a Nicolet iS50 spectrometer (Thermo Fisher Scientific, Waltham, MA, USA) with samples prepared as KBr pellets. XRD patterns were obtained on a Rigaku SmartLab diffractometer (Rigaku Corporation, Akishima, Tokyo, Japan) operating at 45 kV and 100 mA with Cu Kα radiation (λ = 1.5405 Å), scanning from 5° to 90° 2θ at a rate of 10°/min.

2.4. Experimental Procedure and Analytical Methods

To further study the adsorption–desorption performance of Li^+ in real brines, 10 g of Li/Al-LDH–natural mineral composites was added to brines and adsorbed for 3000 min to detect the content of lithium ions in brine and calculate the adsorption capacity. During the desorption process, DI water was selected as the desorption solution. For desorption, the adsorbent was loaded into a glass ion-exchange column and continuously rinsed with DI water until the concentration of lithium in the effluent solution was stabilized.

Each adsorption experiment used 200 mL of LiCl solution (1.8 g·L^{-1}, pH 3.27) with 10 g of adsorbent, corresponding to a solid-to-liquid ratio of 50 g·L^{-1}, shaken at 150 rpm and 30 °C for 48 h to reach equilibrium. For temperature effect studies, the reaction temperature was varied from 25 to 90 °C under otherwise identical conditions. Concentration effect experiments were performed at 30 °C with initial Li^+ concentrations ranging from 0.1 to 3.0 g·L^{-1} for 8 h. To evaluate the influence of pH, the solution pH was adjusted to 3.02,

4.01, 4.91, 6.19, 7.93, and 10.04 using 2 mol·L^{-1} HCl or NaOH, with adsorption carried out at 30 °C for 8 h. The fixed experimental parameters for column desorption tests are listed as follows: column dimensions: inner diameter × height = 15 mm × 300 mm; eluent: deionized water; flow rate: 2 BV·h^{-1}; and total elution volume: 10 BV. The desorption termination criterion was defined as the Li concentration in the effluent being lower than 10 mg·L^{-1}. In the pH-effect adsorption experiments, the solution pH was precisely adjusted using 2 mol·L^{-1} HCl solution (for pH reduction) and 2 mol·L^{-1} NaOH solution (for pH elevation). A calibrated pH meter was used for real-time pH monitoring throughout the adsorption process. Once the solution pH deviated from the preset target value, dilute acid or alkali solution was added dropwise to adjust and stabilize the pH, ensuring a constant pH environment during the whole reaction process.

3. Results and Discussion

3.1. Characterization of Li/Al-LDH–Natural Mineral Composites

To address the hydrodynamic and mass-transfer bottlenecks of powdery lithium adsorbents in fixed-bed applications, a composite granulation strategy was implemented to assemble lithium–aluminum-layered double hydroxides (Li/Al-LDHs) onto three distinct natural clay mineral matrices (Figure 1A). Scanning electron microscopy (SEM) was employed to evaluate the morphological evolution (Figure 1B–E). The unmodified mineral precursors exhibited highly heterogeneous, irregular microstructures. Chlorite presented characteristic stacked sheet structures. Illite appeared as thin, irregularly edged flakes, and montmorillonite exhibited a highly curled, petal-like structure. Following the co-precipitation and granulation process, all three composite adsorbents underwent a clear morphological reorganization, yielding uniform, densely packed, and highly dispersed layered nanostructures. For Chlorite@Li/Al-LDHs (Figure 1B), the parent book-like sheets were uniformly encapsulated by a dense, smooth film of nano-platelets, directly confirming the successful assembly of the LDH active phase. Similarly, Illite@Li/Al-LDHs (Figure 1C) and Montmorillonite@Li/Al-LDHs (Figure 1D) transitioned from their respective irregular and curled raw states into highly ordered, smooth-surfaced layered composite assemblies. While this regularizing trend confirms the universal templating effect of the synthesis, minor morphological nuances were preserved due to the intrinsic structural differences in the parent mineral substrates.

The crystallographic structure and phase purity of the composites were systematically verified by XRD (Figure 1E). All three composites displayed well-resolved, sharp diffraction peaks at 2θ angles of 11.91°, 21.08°, 23.85°, 32.18°, 35.87°, 41.78°, 46.58°, and 49.16°. These reflections precisely match the standard pattern of monoclinic lithium aluminum hydroxide hydrate ($LiAl_2(OH)_7{\cdot}2H_2O$), space group $P2_1/c$, JCPDS card No. 00-040-0710), confirming that the primary active phase in all three systems is highly crystalline Li/Al-LDH [22,23]. Co-existing NaCl peaks were detected across all samples as a reaction byproduct.

Fourier transform infrared (FTIR) spectra (Figure 1F–H) further elucidate distinct interfacial reaction mechanisms [24]. Specifically, the chlorite system (Figure 1F) exhibited remarkable chemical inertness, retaining its primary silicate vibrations while merely anchoring LDH crystallites (~1398 cm^{-1}) via physical interactions [25]. Meanwhile, illite (Figure 1G) underwent mild, localized surface coupling, preserving its core mica-like framework (1026 cm^{-1}) with minor attenuation of edge Si-O bands (750 cm^{-1}) [26]. Lastly, montmorillonite (Figure 1H) demonstrated targeted chemical modification through the selective depletion of edge/interlayer hydroxyls (Al/Mg-OH at 3630 cm^{-1}) without disrupting its underlying 2:1 bulk skeleton [27]. These spectroscopic distinctions collectively confirm that substrate stability dictates the nucleation pathway, ranging from total framework dissolution–recrystallization to surface-confined epitaxial growth.

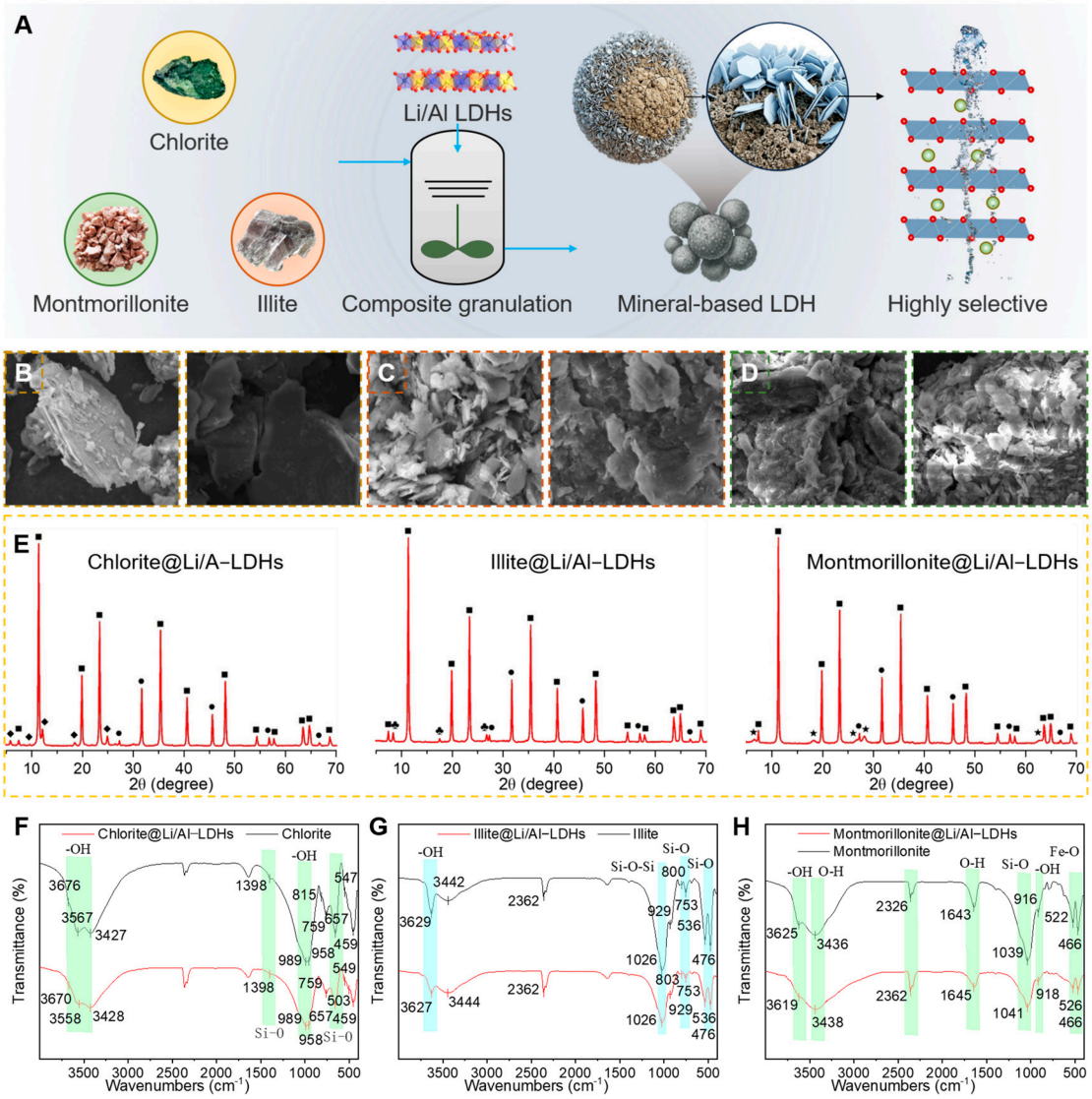


Figure 1. The synthesis scheme and structural characterization of natural mineral-supported Li/Al-LDH composites. (**A**) A schematic representation of the in situ co-precipitation and spherical composite granulation process for fabricating natural mineral-supported Li/Al-LDH adsorbents tailored for continuous selective Li^+ extraction from high Mg/Li ratio brines. Scanning electron microscopy (SEM) images illustrating the microstructural morphologies of the synthesized composites, (**B**) Chlorite@Li/Al-LDHs, (**C**) Illite@Li/Al-LDHs and (**D**) Montmorillonite@Li/Al-LDHs, showcasing the universal transition toward regular, highly dispersed layered architectures. (**E**) X-ray diffraction (XRD) patterns of the three mineral-supported Li/Al-LDH composites. The (■), (♦) (●) (♣) and (★) represent $LiAl_2(OH)_7{\cdot}2H_2O$, $Al_2Si_2O_5(OH)_4$, NaCl, Illite and Montmorillonite. Fourier transform infrared (FTIR) spectra detailing before and after LDH loading for (**F**) chlorite, (**G**) illite, and (**H**) montmorillonite-based composite systems.

The porous architecture and specific surface areas of the mineral-supported Li/Al-LDH composite adsorbents were quantitatively evaluated using nitrogen (N_2) physisorption measurements (Figure 2A–C). All three composite adsorbents display classic Type IV isotherms accompanied by H3 hysteresis loops according to the IUPAC classification (Figure 2A) [28], verifying the presence of slit-like mesoporous networks formed by the interparticle stacking of layered silicate sheets and active LDH crystallites. Quantitative textural parameters obtained from the isotherms and Barrett–Joyner–Halenda (BJH) pore size distributions (Figure 2B,C) reveal substantial structural variations among the three mineral matrices. Illite@Li/Al-LDHs (S_{BET} = 1.80 $m^2{\cdot}g^{-1}$, average pore diameter = 21.34 nm, total

pore volume = 0.009 $cm^3 \cdot g^{-1}$), Chlorite@Li/Al-LDHs (S_{BET} = 1.45 $m^2 \cdot g^{-1}$, average pore diameter = 18.17 nm, total pore volume = 0.0044 $cm^3 \cdot g^{-1}$), and Montmorillonite@Li/Al-LDHs (S_{BET} = 1.16 $m^2 \cdot g^{-1}$, average pore diameter = 4.57 nm, total pore volume = 0.0024 $cm^3 \cdot g^{-1}$) show significantly lower porosity metrics [29]. Notably, the S_{BET} of Illite@Li/Al-LDHs is higher than those of the other two systems, while its pore volume is enlarged by approximately 2 to 5 times. This dramatic enhancement originates from the unique morphology of illite. Its thin and flexible platelets promote uniform dispersion and partial delamination of Li/Al-LDH nanosheets. As a result, a loosely stacked and interconnected three-dimensional porous framework is formed. In contrast, the strong interlayer electrostatic interactions in chlorite, together with the compact structure of montmorillonite, hinder the internal growth of LDH layers. The LDH phase is mainly deposited on external basal surfaces, leading to reduced pore volume and limited mesopore development. The Illite@Li/Al-LDH composite exhibits a dominant mesopore size of 21.34 nm and a high pore volume. These hierarchical porous features provide abundant accessible adsorption sites and facilitate rapid Li^+ diffusion. Consequently, the mass-transfer resistance during continuous-flow lithium extraction is effectively reduced.

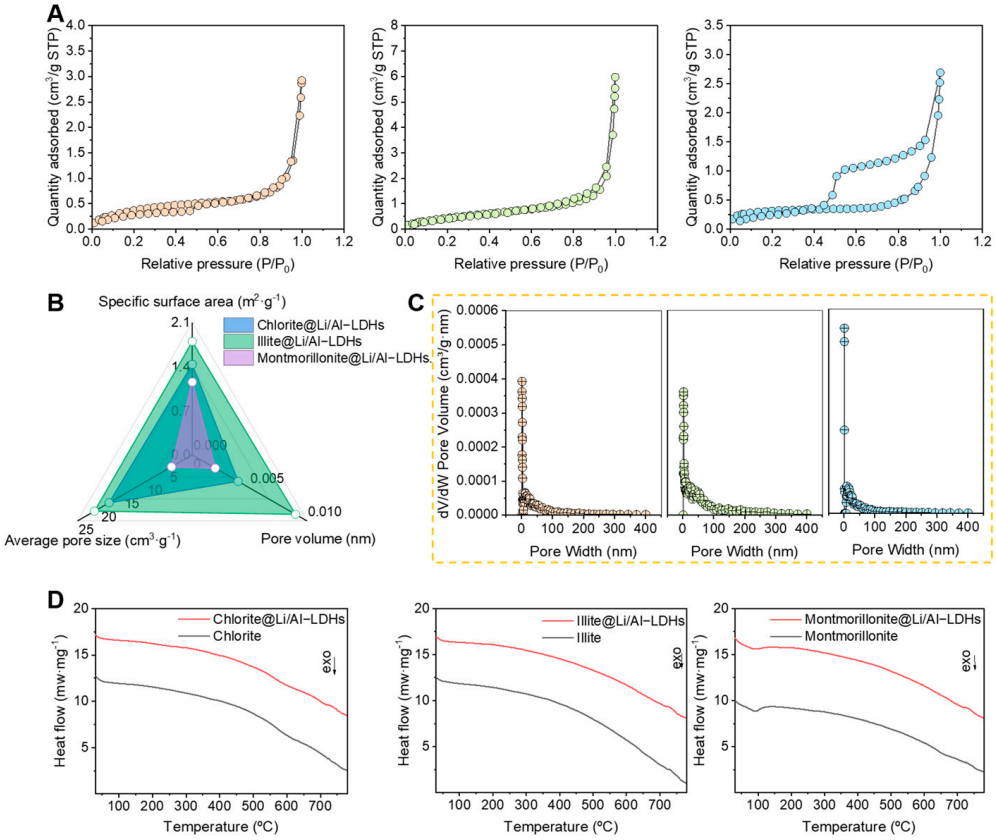


Figure 2. (**A**) N_2 adsorption–desorption isotherms for Chlorite@Li/Al-LDHs, Illite@Li/Al-LDHs, and Montmorillonite@Li/Al-LDHs. (**B**) Radar chart illustrating the comparative textural parameters, including specific surface area (S_{BET}), average pore diameter, and total pore volume, across the three composite adsorbents. (**C**) Pore size distribution curves derived from the Barrett–Joyner–Halenda (BJH) method for the three composites. (**D**) DSC analysis profiles comparing pristine natural minerals with their corresponding Li/Al-LDH composite adsorbents.

The thermal degradation behavior and structural composition of the composites were further investigated by comparing their heat flow profiles with those of raw mineral matrices over a temperature range of 30–780 °C (Figure 2D). Across all systems, the heat flow curves of the LDH-loaded composites display a continuous, monotonic endothermic

decline without sharp phase-transition peaks, signifying overlapping multi-stage endothermic processes including physisorbed water desorption, structural dehydroxylation, and interlayer anion decomposition [30]. Crucially, the incorporation of the LDH phase induces a universal, upward shift in the heat flow profiles. The initial heat flow rate at 30 °C increases from 10–14.5 $mW \cdot mg^{-1}$ for pristine minerals to 17–18 $mW \cdot mg^{-1}$ for the composites, while the residual value at 780 °C rises from 1–2.5 $mW \cdot mg^{-1}$ to 8–9 $mW \cdot mg^{-1}$. This systematic rise reflects a higher density of active hydroxyl groups, interlayer water molecules, and charge-balancing anions introduced per unit mass by the LDH active phase [31]. Among the three matrices, Chlorite@Li/Al-LDHs display a parallel curve shift (pure 12.5 to 2.5 $mW \cdot mg^{-1}$ vs. composite 17 to 9 $mW \cdot mg^{-1}$), indicating additive thermal behavior where the LDH phase is physically anchored atop an intact chlorite core [32]. Similarly, Illite@Li/Al-LDHs (pure 12.5 to 1 $mW \cdot mg^{-1}$ vs. composite 17 to 9 $mW \cdot mg^{-1}$) and Montmorillonite@Li/Al-LDHs (pure 10 to 2 $mW \cdot mg^{-1}$ vs. composite 17 to 9 $mW \cdot mg^{-1}$) combine the thermal stability of their underlying silicate backbones with the high thermal endothermic activity of the surface/interlayer-anchored LDH phases. Significantly, all composites retain elevated heat flow rates at 780 °C, confirming that the LDH-derived active phases possess high thermal stability limits, which is highly advantageous for potential thermal regeneration processes [33].

3.2. Compositional Optimization and Batch Adsorption Performance Dynamics

The mechanical integrity and equilibrium uptake capacity of composite adsorbents are governed by the trade-off between active phase dispersion and structural binder ratio (Figure 3A–C). Across all three systems, increasing the substrate content induces a characteristic "facilitation-then-inhibition" trend, though the optimal threshold and peak performance vary considerably based on the crystallographic architecture of each mineral precursor [34]. In the Chlorite@Li/Al-LDH system (Figure 3A), increasing chlorite content from 8 to 16% enhances the mechanical strength from 76 to 85% and uptake from 2.4 $mg \cdot g^{-1}$ to 3.6 $mg \cdot g^{-1}$ by providing mesoporous scaffolding. Nevertheless, exceeding 16% leads to severe face-to-face sheet aggregation, dropping strength and capacity to 70% and 1.6 $mg \cdot g^{-1}$ at 28% loading due to stress-defect concentration and site encapsulation. Illite@Li/Al-LDHs (Figure 3B) exhibit a similar trend, reaching peak strength (90.1%) and uptake (2.9 $mg \cdot g^{-1}$) at 16% content, as rigid illite plates serve as a structural backbone, whereas higher loading causes dense agglomeration that impedes mass transfer [35]. Montmorillonite@Li/Al-LDHs (Figure 3C) display the broadest processing window, with performance rising from 2.0 $mg \cdot g^{-1}$ (80% strength) at 8% loading to a maximum uptake of 4.6 $mg \cdot g^{-1}$ and exceptional strength of 97% at 18% content [36]. This superior enhancement leverages montmorillonite's swelling ability to generate an open intercalated network. Nevertheless, exceeding 18% loading causes interlayer overcrowding and structural collapse, slightly suppressing adsorption kinetics.

The thermodynamic response to temperature reveals distinct activation mechanisms and mass-transfer characteristics among the three composite systems (Figure 3D–F). Overall, Li^+ uptake increases monotonically with rising temperature across all matrices, confirming the endothermic nature of the adsorption process wherein thermal energy accelerates the thermal motion and diffusion rates of Li^+ within the interlayers. Chlorite@Li/Al-LDHs (Figure 3D), Illite@Li/Al-LDHs (Figure 3E) and Montmorillonite@Li/Al-LDHs (Figure 3F) show continuous capacity increases across 25–90 °C, all reaching equilibrium saturation at 90 °C. Among these three, Montmorillonite@Li/Al-LDHs demonstrate the highest capacity of 6.0 $mg \cdot g^{-1}$ at 90 °C, as thermal expansion uncurls its native petal-like sheets into open diffusion channels [37]. Chlorite@Li/Al-LDHs follow with a maximum capacity of 5.5 $mg \cdot g^{-1}$ at 90 °C due to reduced mass-transfer resistance across the newly formed LDH

surface films. Illite@Li/Al-LDHs deliver the lowest uptake (4.2 mg·g^{-1} at 90 °C) because their tightly stacked, narrow interlayer spacing maintains high mass-transfer resistance even under elevated thermal driving forces.

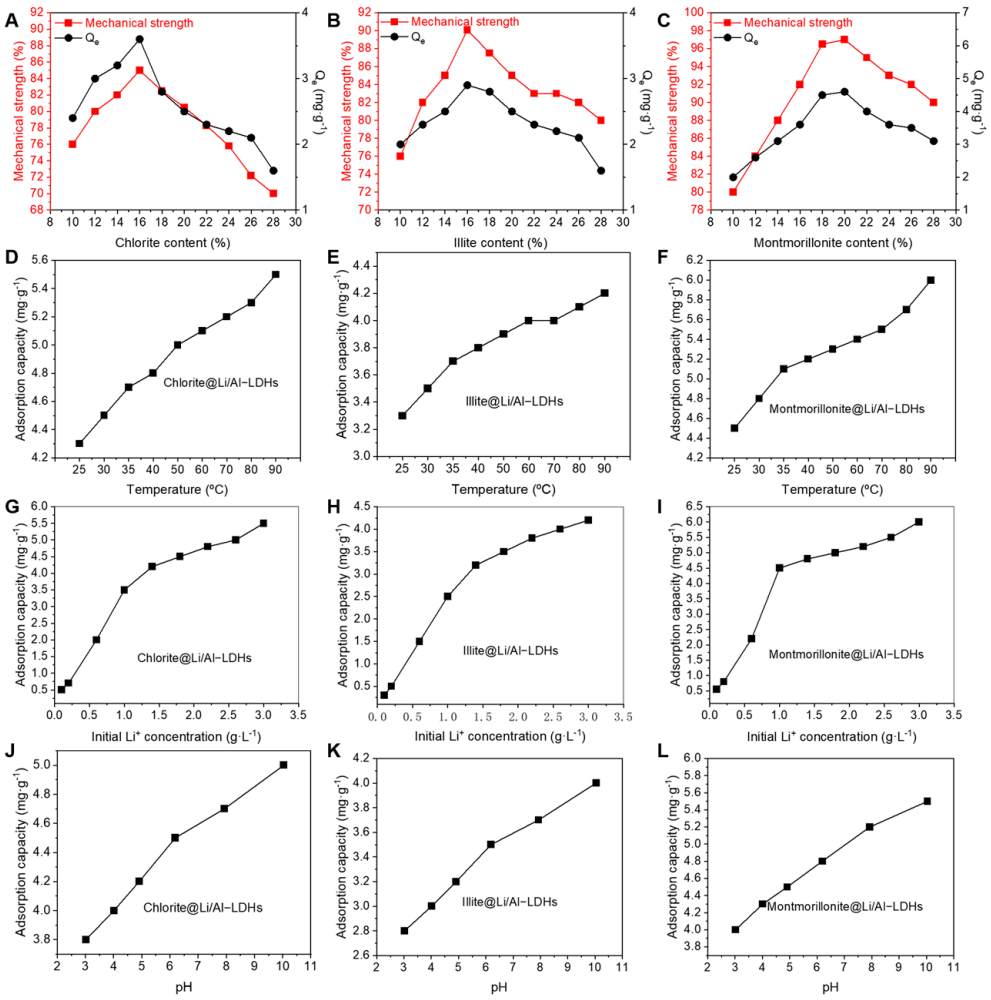


Figure 3. Effect of natural mineral substrate loading content on the mechanical strength and equilibrium Li^+ adsorption capacity of (**A**) Chlorite@Li/Al-LDHs, (**B**) Illite@Li/Al-LDHs and (**C**) Montmorillonite@Li/Al-LDHs. Temperature-dependent Li^+ adsorption behavior across 20–90 °C for (**D**) chlorite, (**E**) illite and (**F**) montmorillonite-supported composite adsorbents. Influence of initial Li^+ concentration on equilibrium uptake for (**G**) Chlorite@Li/Al-LDHs, (**H**) Illite@Li/Al-LDHs and (**I**) Montmorillonite@Li/Al-LDHs. Effect of solution pH (range 3.0–10.0) on Li^+ adsorption capacity for (**J**) Chlorite@Li/Al-LDHs, (**K**) Illite@Li/Al-LDHs and (**L**) Montmorillonite@Li/Al-LDHs.

The effect of initial Li^+ concentration on equilibrium capacity highlights the distribution and availability of active ion-sieve sites (Figure 3G–I). All three composite adsorbents exhibit initial linear uptake increases at lower Li^+ concentrations due to abundant unoccupied active sites, followed by a gradual flattening of the curves as site competition intensifies toward dynamic saturation. Montmorillonite@Li/Al-LDHs (Figure 3I) and Chlorite@Li/Al-LDHs (Figure 3G) display intermediate isotherm profiles, exhibiting linear growth below 1.0 g·L^{-1} and reaching saturation at approximately 3.0 g·L^{-1} with capacities of 6.0 mg·g^{-1} and 5.5 mg·g^{-1}, respectively. Illite@Li/Al-LDHs (Figure 3H) display an inflection point at 1.0 g·L^{-1} and reach saturation at 3.0 g·L^{-1} with the lowest uptake of 4.2 mg·g^{-1}. The influence of solution pH underscores fundamental differences in structural stability and ion-exchange mechanisms (Figure 3J–L). Chlorite@Li/Al-LDHs (Figure 3J), Illite@Li/Al-LDHs (Figure 3K), and Montmorillonite@Li/Al-LDHs (Figure 3L) exhibit op-

posite pH responses, with capacities increasing continuously from pH 3.0 to 10.0 (chlorite: 3.8 to 5.0 mg·g^{-1}, illite: 2.8 to 4.0 mg·g^{-1}, montmorillonite: 4.0 to 5.5 mg·g^{-1}) [38].

3.3. Ion Selectivity and Cycle Stability

The time-dependent uptake profiles and kinetic fitting curves for the three mineral-supported Li/Al-LDH composites demonstrate a universal three-stage kinetic pattern: initial rapid uptake, subsequent mass-transfer-controlled growth, and ultimate equilibrium saturation (Figure 4A–C). For Chlorite@Li/Al-LDHs (Figure 4A), an exponential uptake jump occurs within the first 4 h due to the high density of unblocked, vacant ion-sieve sites in the freshly dispersed adsorbent. From 4 h to 20 h, the adsorption capacity continues to rise smoothly, followed by a gradual flattening beyond 20 h as site availability diminishes and intraparticle mass-transfer resistance increases. The adsorption reached saturation at approximately 12 h, with a maximum equilibrium uptake (q_e) of 5.5 mg·g^{-1}, and remained stable up to 20 h. Near-equilibrium is attained at 20 h, reaching full saturation at 12 h with a maximum equilibrium uptake (q_e) of 5.5 mg·g^{-1}. Across the three systems, the equilibrium saturation times and maximum experimental capacities follow the order: Montmorillonite@Li/Al-LDHs (20 h, 6.0 mg·g^{-1}) > Chlorite@Li/Al-LDHs (20 h, 5.5 mg·g^{-1}) > Illite@Li/Al-LDHs (24 h, 4.2 mg·g^{-1}) (Table 1). To evaluate the effect of the mineral support, a control experiment was performed using unsupported Li/Al-LDHs (synthesized without any mineral support) under identical conditions. As shown in Figure S1, the unsupported Li/Al-LDH powder exhibits significantly lower adsorption capacity (4.0 mg·g^{-1}) compared to the mineral-supported composites (6.0 mg·g^{-1} for Montmorillonite@Li/Al-LDHs), confirming that the mineral support enhances the dispersion and accessibility of the active LDH phase. Kinetic fitting confirms that all three composites adhere significantly better to the pseudo-second-order kinetic model than the pseudo-first-order model. For Chlorite@Li/Al-LDHs, the pseudo-second-order correlation coefficient reaches R^2 = 0.9523, yielding a theoretical equilibrium capacity that closely matches the experimental value. The calculated theoretical capacities for the remaining systems follow the same hierarchy: Montmorillonite@Li/Al-LDHs (5.6513 mg·g^{-1}) > Chlorite@Li/Al-LDHs (5.1116 mg·g^{-1}) > Illite@Li/Al-LDHs (4.0822 mg·g^{-1}). The superior kinetic performance of the pseudo-second-order model confirms that chemisorption, specifically the chemical insertion of Li^+ into the octahedral vacancy sites of the LDH layers, serves as the rate-determining step. The stark differences in capacity and rate stem directly from the microscopic sheet stacking and pore accessibility of the mineral matrices [39]. The open, delaminated polygonal morphology of montmorillonite maximizes active site exposure and minimizes intraparticle diffusion resistance. Conversely, the dense sheet stacking in chlorite generates significant mass-transfer resistance while fine particles plug pore channels, and the rigid, tightly packed illite plates offer the smallest surface area and the highest barrier to Li^+ intercalation. Furthermore, a comparison with previously reported Li/Al-LDH-based adsorbents is provided in Table 2. Our Montmorillonite@Li/Al-LDH composite shows competitive or superior performance relative to most reported systems, demonstrating the advantage of the mineral-directed growth strategy.

The competitive ion-sieve selectivity and distribution coefficients (K_d) were systematically evaluated in complex brine matrices containing abundant competing cations (Mg^{2+}, Na^+, K^+, Ca^{2+}). Across all three tested brines, all composite adsorbents display distribution coefficients following the sequence: K_d (Li^+) >> K_d (Ca^{2+}) > K_d (Mg^{2+}) > K_d (Na^+, K^+) (Figure 4D–F). For Montmorillonite@Li/Al-LDHs, K_d (Li^+) is orders of magnitude higher than those of other cations, yielding separation factors (α_{Me}^{Li}) ranging from 36 to 148.5. Because all α_{Me}^{Li} values are substantially greater than 1, Montmorillonite@Li/Al-LDHs demonstrate exceptional ion-sieve specificity for Li^+ extraction, even in brines with

high Mg^{2+}/Li^{+} ratios of 61.25. While chlorite- and illite-supported adsorbents also exhibit $\alpha_{Me}^{Li} > 1$, their overall selectivity parameters remain inferior to the kaolinite system (Figure 4G–I). This remarkable selectivity originates from a combination of spatial steric hindrance and hydration thermodynamics [20]. The host cavities of the Li/Al-LDH framework precisely match the ionic radius of dehydrated Li^{+} (0.076 nm), whereas larger monovalent and divalent cations (Na^{+}, K^{+}, Ca^{2+}) are excluded by spatial steric constraints. Although Mg^{2+} (0.072 nm) shares a similar ionic radius with Li^{+}, its higher standard hydration free energy creates a formidable energy barrier for dehydration, preventing Mg^{2+} from entering the inner octahedral channels and ensuring high Li^{+} selectivity in high Mg^{2+} brines [40].

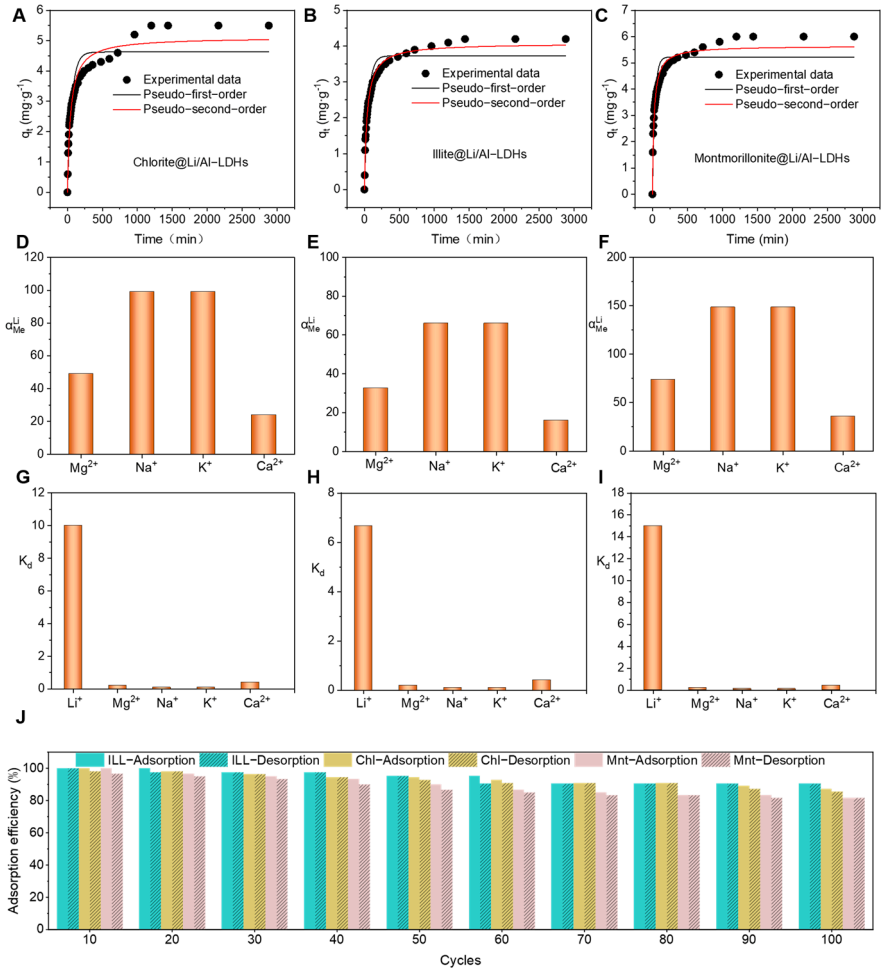


Figure 4. Adsorption kinetic curves fitted with pseudo-first-order and pseudo-second-order models for (**A**) Chlorite@Li/Al-LDHs, (**B**) Illite@Li/Al-LDHs, and (**C**) Montmorillonite@Li/Al-LDHs. Separation factors (α_{Me}^{Li}) for competing metal cations (Mg^{2+}, Na^{+}, K^{+}, Ca^{2+}) across three representative brine solutions for (**D**) chlorite, (**E**) illite, and (**F**) montmorillonite-supported composite adsorbents. Distribution coefficients (K_d) of different metal cations for (**G**) Chlorite@Li/Al-LDHs, (**H**) Illite@Li/Al-LDHs and (**I**) Montmorillonite@Li/Al-LDHs. (**J**) Adsorption capacity retention over 100 consecutive adsorption–desorption cycles using real brine from Qinghai Yiliping Salt Lake.

The long-term operational feasibility and structural stability of the composite adsorbents were evaluated through 100 consecutive adsorption–desorption cycles using raw brine from Qinghai Yiliping Salt Lake under fixed elution conditions (Figure 4J). After 100 complete cycles, the capacity retention rates for the three composite adsorbents are ranked as follows: Chlorite@Li/Al-LDHs (90.5%) > Illite@Li/Al-LDHs (87.3%) > Montmorillonite@Li/Al-LDHs (81.7%). The outstanding cyclic durability highlights their robust framework integrity and chemical stability, which prevents active phase leaching

during repeated water elution. Conversely, the 2:1 expandable layer structure of montmorillonite suffers from lattice expansion–contraction fatigue during cyclic regeneration, resulting in greater structural degradation and capacity loss over extended operation. These results confirm that natural mineral-supported Li/Al-LDHs possess superior mechanical durability, high capacity, and exceptional ion-sieve selectivity, making them a highly promising candidate for practical lithium extraction from high Mg^{2+} brines.

Taken together, the kinetic, selectivity, and cycling results reveal a consistent mechanism. Li^+ uptake is governed by chemisorption through the memory effect, as supported by the pseudo-second-order kinetics and the control experiment with unsupported Li/Al-LDHs. The mineral support enhances the dispersion and accessibility of the active LDH phase, thereby increasing the practical capacity. The high Li^+ selectivity over Mg^{2+} and other cations arises from the size-matching of dehydrated Li^+ within the octahedral vacancies and the high dehydration energy barrier of Mg^{2+}. In addition, the cycling stability is closely related to the structural rigidity of the mineral matrix: chlorite and illite, with more rigid frameworks, provide better capacity retention than the expandable montmorillonite. These findings collectively demonstrate a synergistic mechanism in which the mineral support simultaneously improves capacity, selectivity, and operational stability.

Table 1. Fitting parameters of adsorption kinetic model.

Sample	Pseudo-First-Order			Pseudo-Second-Order		
	q_e (mg/g)	K_1 (L/mg)	R_1^2	q_e (mg/g)	K_2 (L/mg)	R_2^2
Chlorite@Li/Al-LDHs	4.6237	0.01639	0.8661	5.1116	0.00426	0.9523
Illite@Li/Al-LDHs	3.7323	0.01821	0.9233	4.0822	0.00622	0.9860
Montmorillonite@Li/Al-LDHs	5.2225	0.02846	0.8467	5.6513	0.0076	0.9563

Table 2. Comparison of adsorption performance with reported works.

Adsorbents	Adsorption Capacity (mg/g)	Surface Area (m^2/g)	Pore Size (nm)	
Montmorillonite@Li/Al-LDHs	6.0	1.16	4.57	This work
Chlorite@Li/Al-LDHs	5.5	1.45	18.17	This work
Illite@Li/Al-LDHs	4.2	1.8	21.34	This work
BLDH-P [41]	3.95	146	15.23	
GLDH-EA [42]	3.89	46.35	9.09	
R Li/Al-LDH [43]	3.7	32.2	9.13	
GLDH [44]	2.6	280.49	/	

4. Conclusions

In this paper, among the three natural mineral-supported Li/Al-LDH composite adsorbents (chlorite, illite, and montmorillonite) synthesized for selective Li^+ extraction from high Mg^{2+}/Li^+ brines, Montmorillonite@Li/Al-LDHs exhibit vastly superior performance driven by a unique dissolution–recrystallization mechanism during synthesis. This chemical restructuring constructs an open three-dimensional mesoporous framework with a high specific surface area and total pore volume, enabling a maximum equilibrium adsorption capacity of 6.0 $mg \cdot g^{-1}$ that strictly follows pseudo-second-order kinetics. Benefiting from spatial steric size exclusion and the high hydration energy barrier of competing ions, Montmorillonite@Li/Al-LDHs display exceptional ion-sieve selectivity (α_{Me}^{Li} = 36–148.5). Furthermore, optimizing the montmorillonite substrate loading to 20% provides an ideal balance of mechanical strength (97%) and capacity. The Montmorillonite@Li/Al-LDHs can

retain 81.7% of their initial uptake after 100 continuous cycles in raw Qinghai Yiliping Salt Lake brine with a high Mg^{2+}/Li^{+} ratio. These findings confirm montMorillonite@Li/Al-LDHs as a highly durable, efficient, and cost-effective material platform for commercial lithium recovery from high-Mg^{2+}/Li^{+} brines resources.

Supplementary Materials: The following supporting information can be downloaded at: https://www.mdpi.com/article/10.3390/separations13090259/s1, Figure S1: Pure Li/Al-LDHs adsorption scatter plot; Table S1: The ion composition of different concentrations of salt lakes; Table S2: Pre-activation eluent lithium ion concentration; Table S3: Cost budget (10,000 t/a battery-grade lithium carbonate).

Author Contributions: Validation, C.Z., F.Y. and X.M.; Formal analysis, J.G.; Writing—original draft, P.L.; Writing—review & editing, P.L., C.Z., J.G., F.Y. and X.M. All authors have read and agreed to the published version of the manuscript.

Funding: This research received no external funding.

Data Availability Statement: Data will be made available on request.

Conflicts of Interest: Author Fangyuan Yu was employed by the company Jiangsu Suqing Water Treatment Engineering Group Co., Ltd., Jiangyin, China. The remaining authors declare that the research was conducted in the absence of any commercial or financial relationships that could be construed as a potential conflict of interest.

References

1. Xi, H.; Yang, Z.; Liu, Z.; Tang, Y.; Yang, S.; Liu, J.; Iwan, M.; Ibrahim, I.A.; Yin, H. Lithium mining 3.0: Towards a sustainable technology framework for transforming salt-lake brines into clean energy resources. *Renew. Sustain. Energy Rev.* **2026**, *230*, 116704. [CrossRef]
2. Han, S.A.; Kim, H.; Son, J.; Ha, J.; Jo, C. A review of next-generation lithium adsorbents for sustainable extraction from low-concentration resources. *Chem. Eng. J.* **2026**, *532*, 173831. [CrossRef]
3. Wesselkaemper, J.; Renaud, T.; Araya, N.; Dekkers, K.; Popineau, J.; Riffault, J.; O'Sullivan, J.; Haddad, A.Z. Pathways to cost competitive and viable lithium production from Salton Sea geothermal brines. *Nat. Commun.* **2026**, *17*, 8448. [CrossRef] [PubMed]
4. Han, J.; Li, M.; Pang, Z.; Shi, R.; Li, P.; Zhang, Z. Highly stable organic-inorganic composite membrane for selective lithium extraction from high Mg/Li ratio brines: Performance and DFT studies. *Sep. Purif. Technol.* **2026**, *409*, 139262. [CrossRef]
5. Zhang, Y.; Zhang, L.; Bao, S.; Sun, Y.; Chen, B.; Ma, X.; Nie, W.; Liu, C. Lithium and magnesium removal from high Mg/Li ratio brine by electrocoagulation: Processing and mechanism. *Miner. Eng.* **2026**, *248*, 110624. [CrossRef]
6. Feng, T.; Xu, Q.; Sun, B.; Zhang, Y.; Wang, C.; Du, X.; Li, Y.; Gao, F.; Hao, X. Performance and mechanism of ether-based binder (KH-PE) in electrochemically switched ion exchange lithium extraction from salt lake brine with high Mg/Li ratio. *J. Environ. Chem. Eng.* **2026**, *14*, 124017. [CrossRef]
7. Zia, S.; Kashif, M.; Ge, H.; Guo, Y.; Deng, T. Synergistic charge-size trimetallic design PVDF@Mn-co/Al-LDH for efficient lithium selectivity from high-Mg/Li ratio brine. *Desalination* **2026**, *634*, 120327. [CrossRef]
8. Zhang, Z.; Lin, G.; Jiang, H.; Yao, M.; Wang, Q.; Zhang, Y. Dual-modification enabling high-efficiency and stable Li extraction from aluminum-based Lithium ion-sieve. *Chem. Eng. J.* **2026**, *537*, 176456. [CrossRef]
9. Wang, Q.; Hai, C.; Huo, J.; Sun, Y.; Dong, S.; Ma, L.; He, X.; Xu, Q.; Zhou, Y. Preparation of high-load lithium-aluminum layered double hydroxide granules with excellent Li+ adsorption capacity and cycling stability from sulfate type brines. *Water Res.* **2026**, *297*, 125778. [CrossRef] [PubMed]
10. Sotiles, A.R.; Baika, L.M.; Grassi, M.T.; Wypych, F. Cation Exchange Reactions in Layered Double Hydroxides Intercalated with Sulfate and Alkaline Cations $(A(H_2O)_6)[M^{2+}{}_6A_{l3}(OH)_{18}(SO_4)_2]\cdot 6H_2O$ (M^{2+} = Mn, Mg, Zn; A^{+} = Li, Na, K). *J. Am. Chem. Soc.* **2018**, *141*, 531–540. [CrossRef] [PubMed]
11. Cao, Y.; Qiu, C.; Li, J.; Chen, J.; Yu, J.; Lin, S. Dual-phase anion engineering for boosting lithium capture by Li/Al-LDHs. *Desalination* **2026**, *620*, 119646. [CrossRef]
12. Li, T.; Tian, G.; Tian, M.; Xiang, J.; Zhang, L.; Tang, N. A review of Al-based lithium adsorbents for efficient lithium recovery from salty brine: Adsorption mechanism and application progress. *Sep. Purif. Technol.* **2026**, *396*, 137842. [CrossRef]
13. Reich, R.; Slunitschek, K.; Danisi, R.M.; Eiche, E.; Kolb, J. Lithium Extraction Techniques and the Application Potential of Different Sorbents for Lithium Recovery from Brines. *Miner. Process. Extr. Metall. Rev.* **2023**, *44*, 261–280. [CrossRef]

14. Farahbakhsh, J.; Arshadi, F.; Mofidi, Z.; Mohseni-Dargah, M.; Kök, C.; Assefi, M.; Soozanipour, A.; Zargar, M.; Asadnia, M.; Boroumand, Y.; et al. Direct lithium extraction: A new paradigm for lithium production and resource utilization. *Desalination* **2024**, *575*, 117249. [CrossRef]
15. Zhao, C.; Zhang, J.; Zhang, W.; Yang, Y.; Guo, D.; Zhang, H.; Liu, L. Reveal the main factors and adsorption behavior influencing the adsorption of pollutants on natural mineral adsorbents: Based on machine learning modeling and DFT calculation. *Sep. Purif. Technol.* **2024**, *331*, 125706. [CrossRef]
16. Gao, B.; Jang, S.; Son, H.; Park, S.; Lee, H.-S.; Bae, C.-J. Phase transformation and microstructure evolution of a kaolin-based precursor. *Ceram. Int.* **2022**, *48*, 36066–36075. [CrossRef]
17. Huang, P.; Kazlauciunas, A.; Menzel, R.; Lin, L. Determining the Mechanism and Efficiency of Industrial Dye Adsorption through Facile Structural Control of Organo-montmorillonite Adsorbents. *ACS Appl. Mater. Interfaces* **2017**, *9*, 26383–26391. [CrossRef] [PubMed]
18. Wang, X.; Wang, J.; Du, Y.; Wu, J.; Teng, W.; He, H. A diatomite-template self-sacrificing route for Mg-chlorite and its adsorption behavior towards Pb(II)/Cd(II). *Surf. Interfaces* **2022**, *29*, 101775. [CrossRef]
19. Chen, L.; Zhao, Y.; Bai, H.; Ai, Z.; Chen, P.; Hu, Y.; Song, S.; Komarneni, S. Role of Montmorillonite, Kaolinite, or Illite in Pyrite Flotation: Differences in Clay Behavior Based on Their Structures. *Langmuir* **2020**, *36*, 10860–10867. [CrossRef] [PubMed]
20. Wagh, P.; Islam, S.Z.; Lamichhane, T.N.; Bhave, R.R.; Paranthaman, M.P. Separation of Lithium from Aluminum-Containing Clay Mineral Leachate Solution Using Energy-Efficient Membrane Solvent Extraction. *ACS Omega* **2023**, *8*, 46523–46527. [CrossRef] [PubMed]
21. Qin, Y.; Yang, T.; Shi, C.; Liu, B. Adsorption of lithium ions from aqueous solution by magnetic aluminum-based adsorbents. *PLoS ONE* **2023**, *18*, e0295269. [CrossRef] [PubMed]
22. Wu, L.; Li, L.; Evans, S.F.; Eskander, T.A.; Moyer, B.A.; Hu, Z.; Antonick, P.J.; Harrison, S.; Paranthaman, M.P.; Riman, R.; et al. Lithium aluminum-layered double hydroxide chlorides (LDH): Formation enthalpies and energetics for lithium ion capture. *J. Am. Ceram. Soc.* **2019**, *102*, 2398–2404. [CrossRef]
23. Wang, W.; Wang, M.; He, X.; Yang, Y.; Yang, H.; Yanagihara, T. Controllable Synthesis of Organic-Cladding Li/Al-LDH and Its High Cycling Performance for Lithium Extraction from Salt Lakes. *ACS ES&T Water* **2026**, *6*, 1692–1703. [CrossRef]
24. Wang, H.; Feng, Q.; Liu, K. The dissolution behavior and mechanism of kaolinite in alkali-acid leaching process. *Appl. Clay Sci.* **2016**, *132–133*, 273–280. [CrossRef]
25. Hu, F.; Lin, S.; Li, P.; Yu, J. Quantitative Effects of Desorption Intensity on Structural Stability and Readsorption Performance of Lithium/Aluminum Layered Double Hydroxides in Cyclic Li+ Extraction from Brines with Ultrahigh Mg/Li Ratio. *Ind. Eng. Chem. Res.* **2020**, *59*, 13539–13548. [CrossRef]
26. Wungu, T.; Aspera, S.; David, M.; Dipojono, H.; Nakanishi, H.; Kasai, H. Absorption of Lithium in Montmorillonite: A Density Functional Theory (DFT) Study. *J. Nanosci. Nanotechnol.* **2011**, *11*, 2793–2801. [CrossRef] [PubMed]
27. Huo, J.; Hai, C.; Li, Y.; Sun, Y.; Dong, S.; Ma, L.; He, X.; Xu, Q.; Zhou, Y. Configuring a structure self-curable lithium aluminum layered double hydroxide chloride type lithium adsorbents via a facile one-pot synergistical modification way. *Chem. Eng. J.* **2024**, *498*, 155258. [CrossRef]
28. Thommes, M.; Kaneko, K.; Neimark, A.V.; Olivier, J.P.; Rodriguez-Reinoso, F.; Rouquerol, J.; Sing, K.S.W. Physisorption of gases, with special reference to the evaluation of surface area and pore size distribution (IUPAC Technical Report). *Pure Appl. Chem.* **2015**, *87*, 1051–1069. [CrossRef]
29. Rakhsh, F.; Golchin, A. Carbohydrate concentrations and enzyme activities as influenced by exchangeable cations, mineralogy and clay content. *Appl. Clay Sci.* **2018**, *163*, 214–226. [CrossRef]
30. Li, J.; Luo, Q.; Dong, M.; Nie, G.; Liu, Z.; Wu, Z. Synthesis of granulated Li/Al-LDHs adsorbent and application for recovery of Li from synthetic and real salt lake brines. *Hydrometallurgy* **2022**, *209*, 105828. [CrossRef]
31. Altalhi, A.A.; Mohamed, E.A.; Negm, N.A. Recent advances in layered double hydroxide (LDH)-based materials: Fabrication, modification strategies, characterization, promising environmental catalytic applications, and prospective aspects. *Energy Adv.* **2024**, *3*, 2136–2151. [CrossRef]
32. Azizi, K.; Maissara, J.; Chbihi, M.; Youssef, N. Thermal Transformation of Kaolinite Clays: Analyzing Dehydroxylation and Amorphization for Improved Pozzolanic Performance. *Int. J. Chem. Biochem. Sci.* **2024**, *25*, 1070–1077. [CrossRef]
33. Liu, X.; Tang, Y.; Wang, H.; Xia, K.; Meng, Y.; Gong, M.; Li, Z.; Wang, Y. Efficient regeneration and structural transformation pathways observed of LiAl-LDHs adsorbents. *Colloids Surf. A Physicochem. Eng. Asp.* **2026**, *732*, 139180. [CrossRef]
34. Luo, Q.; Dong, M.; Nie, G.; Liu, Z.; Wu, Z.; Li, J. Extraction of lithium from salt lake brines by granulated adsorbents. *Colloids Surf. A Physicochem. Eng. Asp.* **2021**, *628*, 127256. [CrossRef]
35. Zhong, J.; Lin, S.; Yu, J. Li+ adsorption performance and mechanism using lithium/aluminum layered double hydroxides in low grade brines. *Desalination* **2021**, *505*, 114983. [CrossRef]
36. Yotsuji, K.; Tachi, Y.; Sakuma, H.; Kawamura, K. Effect of interlayer cations on montmorillonite swelling: Comparison between molecular dynamic simulations and experiments. *Appl. Clay Sci.* **2021**, *204*, 106034. [CrossRef]

37. Sun, Y.; Yuan, X.; Wen, J.; Yang, Z. The surface and interlayer modification of montmorillonite and its potential application for thermal energy storage. *Renew. Energy* **2024**, *225*, 120282. [CrossRef]
38. Li, Y.; Hai, C.; Huo, J.; Pan, W.; Chen, T.; Li, X.; He, X.; Sun, Y.; Dong, S.; Ma, L.; et al. Performance activation mechanism of aluminum-based layered double hydroxides adsorbents for recovering Li+ by pH modulating. *Chem. Eng. J.* **2024**, *494*, 152919. [CrossRef]
39. Dong, M.; Luo, Q.; Li, J.; Wu, Z.; Liu, Z. Lithium adsorption properties of porous LiAl-layered double hydroxides synthesized using surfactants. *J. Saudi Chem. Soc.* **2022**, *26*, 101535. [CrossRef]
40. Lee, Y.; Cha, J.-H.; Jung, D.-Y. Selective Lithium Adsorption of Silicon Oxide Coated Lithium Aluminum Layered Double Hydroxide Nanocrystals and Their Regeneration. *Chem.—Asian J.* **2021**, *16*, 974–980. [CrossRef] [PubMed]
41. Zhang, L.; Zhang, T.; Lv, S.; Cheng, S.; Dong, G.; Quintana, M.; Song, S.; Zhao, Y. Steering interlayer interaction of lithium-aluminum layered double hydroxide beads for stable lithium extraction from sulfate-type brines. *Desalination* **2024**, *592*, 118130. [CrossRef]
42. Zhang, R.; Yu, J.; Lin, S. An antisolvent extraction strategy for extrusion granulation enhancement of aluminum-based lithium adsorbent used in ultrahigh Mg^{2+}/Li^{+} salt lake brines. *Ind. Eng. Chem. Res.* **2024**, *63*, 2842–2850. [CrossRef]
43. Chen, J.; Du, J.; Yu, J.; Lin, S. A one-step regeneration method in-situ for deactivated aluminum-based lithium adsorbent used in high Mg^{2+}/Li^{+} brines. *Desalination* **2023**, *554*, 116491. [CrossRef]
44. Zhong, J.; Lin, S.; Yu, J. Lithium recovery from ultrahigh Mg^{2+}/Li^{+} ratio brine using a novel granulated Li/Al-LDHs adsorbent. *Sep. Purif. Technol.* **2021**, *256*, 117780. [CrossRef]

Disclaimer/Publisher's Note: The statements, opinions and data contained in all publications are solely those of the individual author(s) and contributor(s) and not of MDPI and/or the editor(s). MDPI and/or the editor(s) disclaim responsibility for any injury to people or property resulting from any ideas, methods, instructions or products referred to in the content.